Full Length Article

Immiscible/Near-Miscible relative permeability for confined fluids at high-pressure and high-temperature for a fractal reservoir

Mingyu Cai [a,b], Yuliang Su [a,b,*], Shiyuan Zhan [c], Derek Elsworth [d], Lei Li [a,b]

[a] *Key Laboratory of Unconventional Oil & Gas Development, Ministry of Education, Qingdao 266580, China*
[b] *School of Petroleum Engineering, China University of Petroleum (East China), Qingdao, Shandong 266580, China*
[c] *College of Energy, Chengdu University of Technology, Chengdu 610059, China*
[d] *Energy and Mineral Engineering & Geosciences, The Pennsylvania State University, University Park, PA 16802, United States*

ABSTRACT

The complex interaction between fluids and solids in reservoirs includes interface slip, capillary confinement and the diffusion and mass transfer between CO_2 and oil and results in intensely nonlinear flow complexity. This study proposes a relative permeability model that accommodates a fractal pore size distribution and honors these complex process interactions. The relative permeability to CO_2 flooding, in the near-miscible region, is predicted through interpolation based on the Gibbs free energy (GFE). The thermodynamic phase behavior of the fluids in the nanopores is considered by applying critical shifts in the temperatures and pressures. A volume-translated Peng-Robinson equation of state is used to calculate the CO_2 and n-alkane densities to high reservoir pressure. Fluid-based correlation and modified volumetric mixing rules are then used to extend the viscosity calculations to mixtures with heavy hydrocarbon components. Predictions from the proposed model better fit experimental observations relative to previous models similarly incorporating fractal theory. The nanopores are shown to increase the relative permeability of the non-wetting phase by decreasing the viscosity ratio of the two phases. Increasing key parameters that are related to the pore structure, e.g. the fractal dimension, D_f, and critical pore radius, r_c, increases the relative permeability of the non-wetting phase. The GFE-based interpolation contributes to the smooth and continuous change in the relative permeability parameters local to the critical point of the mixture, with the confined fluid more likely to be miscible at the same pressure than the bulk fluid. This model can be integrated with a compositional simulator to solve field-scale problems but accommodating the micro-scale physics of unconventional reservoirs.

1. Introduction

The growing proportion of unconventional resources contributing to total hydrocarbon production promotes an increased interest in the physics of fluid-rock interaction in tight oil and shale gas reservoirs [1,2]. Carbon dioxide (CO_2) has been proved to be an effective solvent in EOR to recover oil from unconventional tight-oil and shale-oil reservoirs due to its high solubility and the miscibility with oil [3–5]. Nanopores, as rate-limiting features, comprise the most important pore types in unconventional oil/gas systems as they control the majority storage in tight/shale reservoirs [6,7]. With the decrease in the flow scale, many factors that can be ignored in macro scales gradually play a dominant role in microscale flow [8].

Numerous studies have addressed the effects of nano-confinement on the behavior of the contained fluids and their thermodynamics [9–11]. The static and dynamic behaviors of the fluid is altered at the molecular level in the presence of significant wall-force-field interactions. As a consequence, the mass density distribution is structured and layered within the systems - resulting in spatially varying shear-stress fields and density-dependent fluid-velocity distributions [12]. As the pore diameter of the confining media decreases then pore wall-fluid dispersive interactions become dominant. As a result, the bulk thermodynamic behavior is altered, correspondingly changing coexistence locations, critical properties and the confined fluid density [13,14]. As for the effects of nano-confinement on nonlinear flow, several studies have proposed mathematical models to describe the critical transport mechanisms in tight/shale pores, including boundary layer definition, effective viscosity corrections and slip length evaluations [15–18].

Fractal scaling theory has been widely used to conduct relative permeability curves governing multiphase transport behaviors in nanopores with these critical transport mechanisms [19,20]. Compared with laboratory experiments or numerical methods, which are challengeable and even impossible to obtain relative permeability for the ultra-low-permeability media in tight/shale reservoirs, the analytical models are more flexible and functional [21–24].

However, changes in the oil and rock properties that result from the interaction among CO_2, oil and the solid state reservoir solids, including oil swelling, changes in oil viscosity, CO_2-oil interfacial tension and wettability, together with the extraction of light/intermediate components render it a complex system to accurately characterize for multiphase and multicomponent transport mechanisms. We continue to need an improved understanding of the highly nonlinear displacement and transport processes as they occur at the interplay of phase thermodynamics (phase stability and split) and rock/fluid interaction (relative permeability) [25]. Traditional models rely on phase labels to define the relative permeability parameters such as the endpoints and residual saturations and typically ascribe no dependence on the phase composition. This results in severe discontinuities in the relative-permeability *versus* phase-saturation relationships and in severe numerical instabilities and increased computational time [26]. To alleviate this issue, models have been introduced that are based on phase state indicators (e. g., interfacial tension, parachor, GFE) [27–29]. The hydrocarbon relative permeability can then be interpolated between the gas-like and oil-like relative-permeability curves by using interpolation functions that are related to these phase state indicators.

Numerical results, recovered with such adjustments, show significant improvements in the nonlinear convergence with compositional dependencies enforced in the relative permeability near the critical point. However, the effects of the nanopore confinement on the multiphase and multicomponent transport mechanisms have not been previously included. This impact will be significant for nanoporous media where pore confinement effects are strong. We explore this behavior with a new relative permeability model to describe the nonlinear multiphase flow in nanoporous media with the coexistence of oil, gas, and water. Water exists only as a mono-molecular wall-bonded film that regulates liquid–liquid slip velocity of oil–water in the proposed physical model. Fractal theory is then applied to define the immiscible fluxes of oil and gas in the porous medium. Both fluid properties and vapor–liquid equilibrium (VLE) under a high pressure and temperature are calculated by combining the volume-translated Peng-Robinson equation of state (VTPR EOS) with the expanded fluid theory (EFT) of the viscosity correlation. Thermodynamic phase changes of the fluids inhabiting the nanopores are also included in the VLE calculation to clarify the effect of pore-wall proximity on the molecular response. Relative permeability for the near-miscible state is estimated from normalized Gibbs free energy (GFE) based interpolation.

2. Model and methodology

2.1. Multiphase transport in a confined space

Molecular simulations have confirmed that a single/mono-molecular layer of water film (WF) can form on the surface of inorganic matter (i.e., quartz) due to the high affinity of the hydrogen bonds. The WF can significantly influence the surface properties, such as the oil adsorption, mobility, contact angle, and transport behavior [30,31]. The slip boundary condition is particularly important in describing the hydrocarbon transport in nanopores [32]. Moreover, a weakly ordered structure of the liquid hydrocarbon (C_{8+}) and a sharp change in the velocity profiles in the oil–water interface regions are observed, indicating the existence of liquid–liquid slip in the oil–water interface region [32,33]. According to the physical properties of both the static pore walls and the mobile fluids, we make the following assumptions. That: (1) the pore surfaces are water-wet, (2) the solubility of CO_2 in water is

negligible, (3) the water phase exists only as immobile bound or adsorbed water, (4) liquid–liquid slip occurs between water and the bulk oil, and 5) and a CO_2-oil transition zone exists due to gas dissolution and diffusion. A schematic of the proposed model is shown in Fig. 1.

Fig. 1. Axisymmetric multiphase flow within a parallel-sided capillary. R_1 is the radius of the total flowing section. R_2 is the radius of the gas area (including the transition zone and bulk gas zone). In addition, l_0, l_1, and l_2 represent the thickness of the adsorbed water, bulk oil zone, and oil–gas transition.

2.2. Density and viscosity calculation

The criticalities of the components (including the critical temperature, T_c, critical pressure, P_c, and critical specific volume, V_c) in the confined pore are modified to correspond to a prescribed pore diameter r_p. The thermodynamic phase changes of the nanopore fluids are given as [9]:

$$T_c = \frac{8}{27bR}\left[a - 2\sigma^3 \varepsilon N^2 \frac{\sigma}{r_p}\left(c_1^{con} + c_2^{con}\frac{\sigma}{r_p}\right)\right] \tag{1}$$

$$P_c = \frac{1}{27b^2}\left[a - 2\sigma^3 \varepsilon N^2 \frac{\sigma}{r_p}\left(c_1^{con} + c_2^{con}\frac{\sigma}{r_p}\right)\right] \tag{2}$$

$$V_c = 3b \tag{3}$$

where a and b represent the van der Waals (vdW) energy parameters; σ and ε represent the Lennard-Jones size and energy parameters, respectively; N is Avogadro's number; and c_1^{con} and c_2^{con} are recovered as 2.6275 and -0.6743 from data regressions.

The volume-translated Peng-Robinson equation of state (VTPR EOS) [34,35] is applicable to calculate the fluid density for the saturated- and single-phase regions of the pure fluids at high pressures. By using conventional mixing rules, Abudour et al. [36] extended the volume-translation method to predict the densities of the liquid mixtures over a large range of pressures and temperatures to mixtures. From this, the volume-translation term for the equation of state is given as [36,37]:

$$v_{VTPR} = v_{PR} + c_m - \delta_{c_m}\left(\frac{0.35}{0.35 + d_m}\right) \tag{4}$$

where,

$$c_m = \left(\frac{RT_{c_m}}{P_{c_m}}\right)\left[c_{1m} - \left(0.004 + c_{1m}^v\right)exp\left(-2d_m\right)\right] \tag{5}$$

$$d_m = \frac{1}{RT_{c_m}}\left(\frac{\partial P^{PR}}{\partial \rho}\right)_T - \left(\frac{1}{RT_{c_m}\rho^2}\right)\frac{a_{v1}^2}{a_{11}} \tag{6}$$

$$\delta_{c_m} = v_{c_m}^{PR}(x) - v_{c_m}(x) \tag{7}$$

$$c_{1m}^v = \sum x_i c_{1i}^v \tag{8}$$

$$v_{c_m}^{PR}(x) = \left(\frac{RT_{c_m}}{P_{c_m}}\right)\left(z_c^{EOS}\right) \tag{9}$$

T_{c_m} is the critical temperature of the mixture, P_{c_m} is the critical pressure of

the mixture, and z_c^{EOS} is fixed at 0.3074 from the critical point condition for the PR-EOS [38,39]. c_{1i}^v is a species-dependent parameter that can be generalized in terms of the critical compressibility factor of each fluid, Z_{ci}, as [40]:

$$c_{1i}^v = 0.4266 Z_{ci} - 0.1101 \tag{10}$$

The true critical volume of the mixture is estimated by applying the following expressions [36,41].

$$v_{c_m}(x) = \sum_i \theta_i v_{c_i} \tag{11}$$

$$\theta_i = \frac{x_i v_{c_i}^{2/3}}{\sum_i x_i v_{c_i}^{2/3}} \tag{12}$$

where v_{c_i} represents the critical volume of the pure compound i, θ_i is the surface fraction of compound i, and x_i is the mole fraction of compound i. Then, the mixture critical temperature is written as [41]:

$$T_{c_m} = \sum_i \theta_i T_{ci} \tag{13}$$

The mixture critical pressure can then be determined as [42].

$$P_{c_m} = \frac{(0.2905 - 0.085\omega_m)RT_{c_m}}{v_{c_m}} \tag{14}$$

$$\omega_m = \sum_i x_i \omega_i \tag{15}$$

where ω_m is the mixture acentric factor and ω_i is the acentric factor of compound i. In this work, the critical properties of the fractions are calculated with the Lee-Kesler correlations [43], which is based on the same theoretical assumption as Eq. (14) (using Lee-Kesler equation of state [44]). Thus, the mixing rule of Eq. (14) is applicable for the fluids in the pores from the large scale (without confinement) to the microscale (with confinement). The fitting progress can induce an adjustable critical volume $v_c^{'}$ for the components to eliminate the additional deviation of the adjustment of some pseudo-component properties. Then, applying the approximation in Eq. (14) will not affect the calculations in other parts of this work.

An expanded fluid-based (EFB) correlation is used to calculate the fluid viscosity so that the model is suitable for many n-alkanes, branched alkanes, and other hydrocarbon mixtures from [45]:

$$\mu - \mu_G = c_1 [\exp(c_2 \beta) - 1] \tag{16}$$

$$\beta = \frac{1}{exp\left[\left(\frac{\rho_s^*}{\rho}\right)^n - 1\right]} - 1 \tag{17}$$

$$\rho_s^* = \frac{\rho_s^0}{1 - c_4[1 - exp(-c_3 P)]} \tag{18}$$

where μ and μ_G represent the fluid and dilute gas viscosity, respectively, and ρ_s^* and ρ represent the fluid density in the compressed state and for the target system, respectively. In addition, the universal constants c_1 and n are derived to be 0.4214 and 0.4872, based on the minimization of the error in viscosity [45,46]. c_2 is a dimensionless fitting parameter for each pure component as recovered from the regression of some observations [45], while μ_{25c} is the viscosity at 25 °C. An extensive statistical analysis shows that ρ_s^* can be calculated by applying Eq. (18) that relates to the pressure, P, the compressed state density in a vacuum, ρ_s^0, and the adjustable parameters c_3 and c_4 [45]. Typically, c_3 and c_4 are related to the component molar weight, MW as:

$$c_3 = 1.435 \times 10^{-6} MW^{0.4267} \tag{19}$$

$$\begin{cases} c_4 = 0.015 + 0.00042|50 - MW|; MW \leq 97 \\ c_4 = 0.035; MW > 97 \end{cases} \tag{20}$$

However, for heavier n-alkanes, if $c_3 > 2.8 \times 10^{-7}$, then Eq. (19) can be rewritten as [47]:

$$c_3 = \frac{2.8 \times 10^{-7}}{1 + 3.23 \times exp(-1.54 \times 10^{-2} MW)} \tag{21}$$

The components of the mixture may be treated as an overall system, and modified and simple volumetric mixing rules [48,49] are combined to extend the correlation to the mixtures, as:

$$\rho_{s,mix}^0 = \left(\sum_{i=1}^N \sum_{j=1}^N \frac{m_i m_j}{2} \left(\frac{1}{\rho_{s,i}^0} + \frac{1}{\rho_{s,j}^0} \right) (1 - \beta_{ij}) \right)^{-1} \tag{22}$$

$$\frac{c_{2,mix}}{\rho_{s,mix}^0} = \sum_{i=1}^N \sum_{j=1}^N \frac{m_i m_j}{2} \left(\frac{c_{2,i}}{\rho_{s,i}^0} + \frac{c_{2,j}}{\rho_{s,j}^0} \right) (1 - \beta_{ij}) \tag{23}$$

$$\begin{cases} c_{3,mix} = 1.435 \times 10^{-6} \sum_{i=1}^N (z_i MW_i)^{0.4267}; c_{3,mix} \leq 2.8 \times 10^{-7} \\ c_{3,mix} = \frac{2.8 \times 10^{-7}}{1 + 3.23 \times exp\left[-1.54 \times 10^{-2} \sum_{i=1}^N (z_i MW_i)\right]}; c_{3,mix} > 2.8 \times 10^{-7} \end{cases} \tag{24}$$

$$\begin{cases} c_{4,mix} = 0.015 + 0.00042 \times \left|50 - \sum_{i=1}^N (z_i MW_i)\right|; \sum_{i=1}^N (z_i MW_i) \leq 97 \\ c_{4,mix} = 0.035; \sum_{i=1}^N (z_i MW_i) \rangle 97 \end{cases} \tag{25}$$

where N is the number of components, m is the mass fraction of the pure component in the mixture, β_{ij} is a binary-interaction parameter, and z is the molar fraction of a pure component in the mixture.

2.3. Relative permeability model

The flow velocity in the region of adsorbed water remains zero. However, the surface is in contact with the oil region and this can promote oil flow through liquid–liquid slip. The velocity of the bulk oil, v_o, the oil–gas transition fluid, v_{og}, and the bulk gas, v_g, can be expressed through Eqs. (26), (27), and (28), respectively, as:

$$v_o(r) = \frac{\Delta P}{L} \frac{R_1^2 - r^2}{4\mu_o} + C_1, R_2 < r \leq R_1 \tag{26}$$

$$v_{og}(r) = \frac{\Delta P}{L} \frac{R_1^2 - r^2}{4\mu_{og}} + C_2, R_3 < r \leq R_2 \tag{27}$$

$$v_g(r) = \frac{\Delta P}{L} \frac{R_1^2 - r^2}{4\mu_g} + C_3, 0 < r \leq R_3 \tag{28}$$

where: r represents the distance from the midline of the capillary; μ_o, μ_{og}, and μ_g represent the viscosity of the bulk oil, transition zone fluid, and bulk gas, respectively. Similarly, C_1, C_2, and C_3 are the correction factors that are associated with the liquid–liquid slip and fluid viscosity. The boundary conditions are prescribed as:

$$v_o|_{r=R_1} = v_{slip} \tag{29}$$

$$v_o|_{r=(R_1-l_1)} = v_{og}|_{r=(R_1-l_1)} \tag{30}$$

$$v_{og}\big|_{r=(R_2-l_2)} = v_g\big|_{r=(R_2-l_2)} \tag{31}$$

$$\frac{\partial v_g}{\partial r}\bigg|_{r=0} = 0 \tag{32}$$

The slip velocity may be determined by applying the relations [32]:

$$v_{slip} = \frac{\tau}{\beta} \tag{33}$$

where β is the liquid–liquid slip coefficient (0.612 ± 0.057 MPa•s/m), and τ is the oil–water interface shear stress, which can be calculated by using the relations [50,51]:

$$\tau = f \cdot \frac{1}{2}\rho_o(v_{oc} - v_w)^2 \tag{34}$$

$$f = Bm\left(\frac{d_c v_{0c} \rho_o}{\mu_o}\right)^{-n} \tag{35}$$

where f is the interfacial friction coefficient; v_{oc} is the average velocity of the bulk oil without liquid–liquid slip; $d_c = 2R_1$, ρ_o is the oil density; and n and m represent the Reynolds number correction parameters, which are typically $n = 1$ and $m = 16$ for laminar flow. B is an additional parameter that ranges from 0.8 to 1 with $B = 1$ when there is only a slight waviness at the oil–water interface. Since we ignore the flow of the adsorbed WF, Eq. (34) can be expressed as:

$$\tau = \frac{4\mu_o v_{0c}}{R_1} = \frac{\Delta P}{L}\frac{R_1^2 - r^2}{R_1} \tag{36}$$

Substituting Eqs. (26), (27), and (28) into Eqs. (29), (30), and (31), results in the following correlation factors:

$$C_1 = \frac{\tau}{\beta} = \frac{\Delta P}{L}\frac{R_1^2 - r^2}{\beta R_1} \tag{37}$$

$$C_2 = \frac{\Delta P}{L}\left[\frac{R_1^2 - R_2^2}{4\mu_0} - \frac{R_1^2 - R_2^2}{4\mu_{0g}}\right] + \frac{\tau}{\beta} \tag{38}$$

$$C_3 = \frac{\Delta P}{L}\left[\frac{R_1^2 - R_2^2}{4\mu_o} + \frac{R_2^2 - R_3^2}{4\mu_{og}} - \frac{R_1^2 - R_3^2}{4\mu_g}\right] + \frac{\tau}{\beta} \tag{39}$$

allowing, Eqs. (26), (27), and (28) to be rewritten as:

$$v_o(r) = \frac{\Delta P}{L}\frac{R_1^2 - r^2}{4\mu_o}\left(1 + \frac{4\mu_o}{\beta R_1}\right), R_2 < r \leq R_1 \tag{40}$$

$$v_{og}(r) = \frac{\Delta P}{L}\left(\frac{R_1^2 - R_2^2}{4\mu_o} + \frac{R_2^2 - r^2}{4\mu_{og}} + \frac{R_1^2 - r^2}{\beta R_1}\right), R_3 < r \leq R_2 \tag{41}$$

$$v_g(r) = \frac{\Delta P}{L}\left(\frac{R_1^2 - R_2^2}{4\mu_o} + \frac{R_2^2 - R_3^2}{4\mu_{og}} + \frac{R_3^2 - r^2}{4\mu_g} + \frac{R_1^2 - r^2}{\beta R_1}\right), 0 < r \leq R_3 \tag{42}$$

where $R_1 = r$, $R_2 = r - l_1$, and $R_3 = r - l_1 - l_2$. The values of l_1 and l_2 are related to the molar fraction of the hydrocarbons and CO_2 components and the degree of miscibility. The higher the CO_2 concentration in the displacement phase, the thicker the oil–gas transition zone under the same pressure, with a minimum l_2 of ~ 15 Å in the immiscible state. The width ratio R_3/l_1 is equal to the gas–liquid ratio that is calculated from the VTPR equation of state, as V_g/V_L. Then, we can calculate the flow velocities of the gas, liquid, and transition zone with the outflow radius of R_1 from Eqs. (40), (41), and (42).

The volumetric fluxes of the different zones are calculated by the following integral.

$$q_o = \int_{R_2}^{R_1}\frac{\Delta P}{L}\frac{R_1^2 - r^2}{4\mu_o}\left(1 + \frac{4\mu_o}{\beta R_1}\right) \cdot 2\pi r dr = \frac{\Delta P}{L}\frac{\pi}{8\mu_o}\left(1 + \frac{4\mu_o}{\beta R_1}\right)\left(R_1^2 - R_2^2\right)^2 \tag{43}$$

$$q_{og} = \int_{R_3}^{R_2}\frac{\Delta P}{L}\left(\frac{R_1^2 - R_2^2}{4\mu_o} + \frac{R_2^2 - r^2}{4\mu_{og}} + \frac{R_1^2 - r^2}{\beta R_1}\right) \cdot 2\pi r dr$$

$$= \frac{\Delta P}{L}\frac{\pi}{2}\left[\frac{\left(R_1^2 - R_2^2\right)\left(R_2^2 - R_3^2\right)}{2\mu_o} + \frac{\left(R_2^2 - R_3^2\right)^2}{4\mu_{og}} + \frac{\left(R_2^2 - R_3^2\right)\left(2R_1^2 - R_2^2 - R_3^2\right)}{\beta R_1}\right] \tag{44}$$

$$q_g = \int_0^{R_3}\frac{\Delta P}{L}\left(\frac{R_1^2 - R_2^2}{4\mu_o} + \frac{R_2^2 - R_3^2}{4\mu_{og}} + \frac{R_3^2 - r^2}{4\mu_g} + \frac{R_1^2 - r^2}{\beta R_1}\right) \cdot 2\pi r dr$$

$$= \frac{\Delta P}{L}\frac{\pi R_3^2}{2}\left(\frac{R_1^2 - R_2^2}{2\mu_o} + \frac{R_2^2 - R_3^2}{2\mu_{og}} + \frac{R_3^2}{4\mu_g} + \frac{2R_1^2 - R_3^2}{\beta R_1}\right) \tag{45}$$

Assuming that the pore radii obey a fractal distribution, then the number of pores in the range from r to $r + dr$ can be determined by applying Eq. (46) as [52]:

$$-dN = D_f r_{max}^{D_f} r^{-(D_f+1)} dr \tag{46}$$

The average pore radius can then be calculated by using [53]:

$$r_{mean} = E(r) = \int_{r_{min}}^{r_{max}} D_f r_{max}^{D_f} r^{-D_f} dr \tag{47}$$

and total volume fluxes of oil and gas expressed as:

$$Q_o = \int_{r_{min}}^{r_{max}}\left(q_o + M_{vo} q_{og}\right)dN \tag{48}$$

$$Q_g = \int_{r_{min}}^{r_{max}}\left[q_g + (1 - M_{vo})q_{og}\right]dN \tag{49}$$

For the wetting phase flux, such as the oil phase Q_o in the coexistence system, this involves an additional resistance factor β_R [54] that is equal to the reciprocal of the wetting phase saturation S_{wet}, which is based on the fitting results in this study. To ensure continuity in the change in viscosity with radius, the mole fraction ratio of the oil to CO_2 in the transition zone is defined as:

$$M_{vo} = \frac{l_2\left(-1 + 2\sum_{i=1}^{N_c} z_i\right)}{2R_1} + \frac{1}{2} \tag{50}$$

where z_i is the mole fraction of the hydrocarbon component, i is the component number, and N_c represents the total number of hydrocarbon components.

The saturation of the oil phase (relative wetting phase) saturation can be expressed as:

$$S_{or} = \frac{\int_{r_{min}}^{r_c}\pi r^2 dN + \int_{r_c}^{r_{max}}\pi\left[R_1^2 - R_2^2 + M_{vo}\left(R_2^2 - R_3^2\right)\right]dN}{\int_{r_{min}}^{r_{max}}\pi r^2 dN}$$

$$= \frac{\frac{\left(r_c^{2-D_f} - r_{min}^{2-D_f}\right)}{(2-D_f)} + \int_{r_c}^{r_{max}}\left[R_1^2 - R_2^2 + M_{vo}\left(R_2^2 - R_3^2\right)\right]dr}{\left(r_{max}^{2-D_f} - r_{min}^{2-D_f}\right)/\left(2 - D_f\right)} \tag{51}$$

When the pore diameter is smaller than the critical pore radius, r_c, then gas is excluded by the magnitude of the capillary force - the pore space is then fully occupied by oil. To define the initial state of immiscibility, r_c may be recovered from a core displacement experiment. However, r_c decreases as the system approaches miscibility. When calculating the oil and gas saturation, both the adsorbed water and trapped water are assumed to exist at irreducible water saturation S_{wc}. From this, the oil and gas saturation can be obtained as:
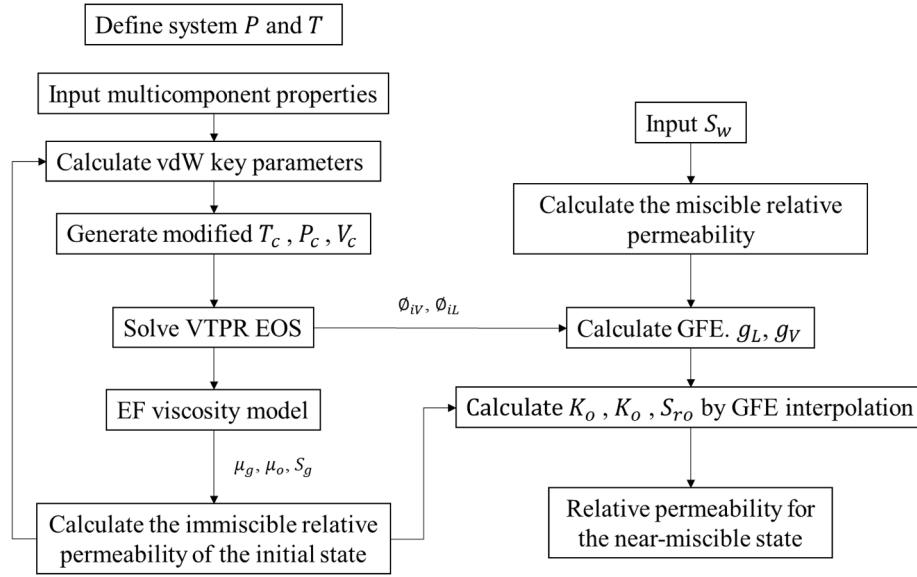
Fig. 2. Flowchart for estimating immiscible and near-miscible relative permeabilities.

$$S_g = (1 - S_{wc})(1 - S_{or}) \qquad (52)$$

$$S_o = (1 - S_{wc})S_{or} \qquad (53)$$

According to an expanded version of Darcy's Law, the effective permeabilities of the oil and gas phase are defined as [55]:

$$k_o = S_o \frac{\phi Q_o \mu_o L}{A_P \Delta P} \qquad (54)$$

$$k_g = S_g \frac{\phi Q_g \mu_g L}{A_P \Delta P} \qquad (55)$$

where A_P is the cross-sectional area of the pore and ϕ is the porosity. To ensure that the phase permeability endpoint value is less than 1, the absolute permeabilities are calculated by the maximum oil and gas flux, which are Q_{ot} and Q_{gt}, respectively, and defined as:

$$k_{abs\_o} = \frac{\phi Q_{ot} \mu_o L}{A_P \Delta P} \qquad (56)$$

$$k_{abs\_g} = \frac{\phi Q_{gt} \mu_g L}{A_P \Delta P} \qquad (57)$$

The relative permeability is then obtained from Eqs. (58) and (59).

Fig. 3. Fitting of proposed model against observations from both core-flooding experiments [64,65] and analytical simulation [60].

$$k_{ro} = \frac{k_o}{k_{abs\_o}} \qquad (58)$$

$$k_{rg} = \frac{k_g}{k_{abs\_g}} \qquad (59)$$

Since the fugacity, f_i, for each component can be calculated by applying a two-phase flash by using PR-EOS with the modifications in Section 2.3, the normalized Gibbs free energy (NGFE) can be obtained as [22,56]:

$$g_l^* = \frac{G_l}{RT} = \sum_{i=1}^{N} x_i ln(f_{li}) \qquad (60)$$

$$g_v^* = \frac{G_v}{RT} = \sum_{i=1}^{N} y_i ln(f_{vi}) \qquad (61)$$

The relative permeability curves in the immiscible state can be calculated for the wellhead condition (101.325 KPa, 25℃), while the relative permeability curves in the completely miscible state are intersecting straight lines with endpoints that are associated with an immobile saturation. Then, the relative permeability parameters can be linearly interpolated by using the current GFE between the two reference states [22,57]:

$$k_{rp}^{Cor} = F_k \cdot k_{rp}^{Imm}(S_p) + [1 - F_k] \cdot k_{rp}^{Mis}(S_p) \qquad (62)$$

where k_{rp}^{Imm} and k_{rp}^{Mis} represent the immiscible and miscible curves, and S_p is the saturation of phase p. The interpolation parameter, F_k, varies from zero at complete miscibility to unity for immiscible displacement and may be evaluated from Eq. (63) [22]:

$$\begin{cases} F_k = 1 - max\left(\frac{g_l^*}{g_v^*}, 0\right)^n, np = 2(a) \\ \\ F_k = 1 - max\left[\frac{min(g_c^*, g_0^*)}{max(g_c^*, g_0^*)}, 0\right]^n, np = 1(b) \end{cases} \qquad (63)$$

where np represents the total system phase number, g_c^* is the normalized Gibbs free energy for the target system, and g_0^* is the normalized Gibbs free energy at the critical point.

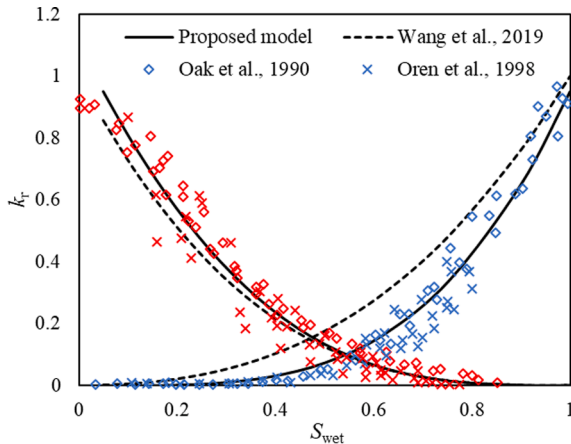An operational flowchart describing the proposed model is shown in Fig. 2.
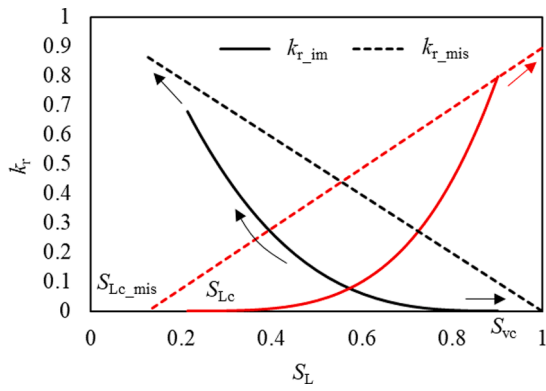
Fig. 4. Relative permeability for two reference points representative of the immiscible and miscible states.
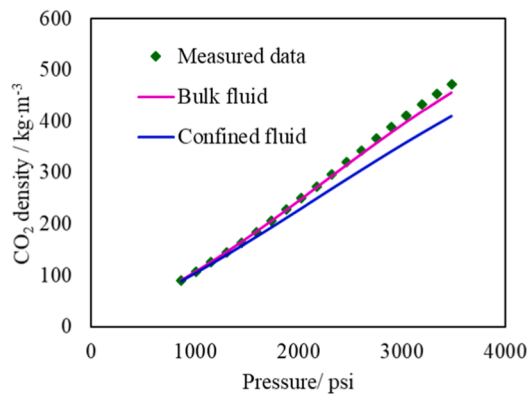
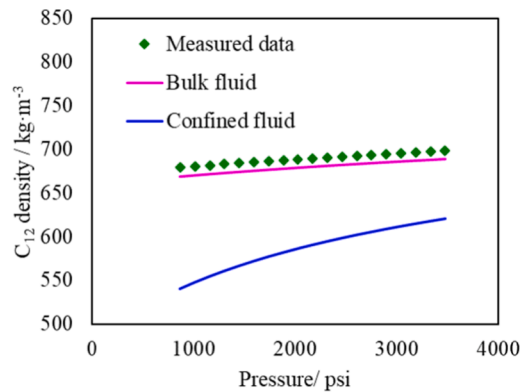## 3. Results and discussion

3.1. Model validation

Fractal theory has been broadly applied to describe relative permeability in immiscible two-phase/three-phase systems [58,59]. Models have been variously validated against experimental studies, Lattice Boltzmann simulations and several widely used semi-empirical models [60,61]. Traditional experiments are restricted to provide observations of only averaged relative permeabilities [62]. Lattice Boltzmann methods may define spatial distributions of fluxes but are challenged by the need to accurately define geometry at fine-resolution and only return the physics that is included in the model [63]. Correspondingly, we simplified the proposed model to a completely immiscible system by specifying a fixed viscosity ratio ($\frac{\mu_{non\_wet}}{\mu_{wet}} = 0.75$), a defined no-slip boundary ($v_{slip} = 0$), and equal phase fraction in the transition zone ($M_{vo} = \frac{1}{2}$) to allow verification, as shown in Fig. 3. Compared with prior results from Wang et al. [60] (dotted line), the proposed model considers the impact of near-wall flow resistance. This results in a lower wetting phase relative permeability that ultimately provides a better fit with experimental observations [64] (scattered points). It should be noted that the value of the additional resistance coefficient β_r may be changed with the contact angle and the morphology of the pore surface [65]. Thus, more tests can be conducted to determine β_r for the different formations if necessary.

3.2. Relative permeability modeling

A sample of oil recovered from the Wolfcamp formation in Apache's Lin field is used in this study [66]. Defined characteristics of the oil sample include the composition (m), critical temperatures and pressures (T_c, P_c), the acentric factor (a_c), molar weight (M_w), and various calculated parameters, including the vdW energy and volume parameter (a, b), the Lennard-Jones energy parameter (ε), and the criticalities of temperature and pressure after modification ($T_c^{'}$, $P_c^{'}$) are shown in Table 1 (in the Appendix). Table 2 (in the Appendix) presents the binary-interaction parameters in the modified flash calculation model.

The minimum miscible pressure (MMP) of the oil sample was calculated to be 3,425 psi by traditional cell-to-cell simulation [67,68] at a reservoir temperature of 255 °F. This is slightly lower than the reservoir pressure of 3,450 psi, which indicates that miscibility with multiple contacts is attainable while remaining at a near-miscible state in most cases. Typically, the reference relative permeability parameters are based on experimental data, and interpolations are then conducted between them based on a function that is related to the GFE. Selection of the reference values has been discussed in detail elsewhere [27,29] and is not repeated here. In this study, one reference value is the GFE that was calculated for the injection components (16.89 for pure CO_2) when the pressure first results in miscibility (FCM), which was 4,700 psi. The other reference value for the immiscible state is the calculation result for the separated oil (5.977) with an original CO_2 fraction of 0.99 at the bottom hole pressure of the producing well (1500 psi). The selected reference states span a sufficiently wide bracket that all interpolations during CO_2 flooding fall intermediate to these limits. As shown in Fig. 4, the x-coordinate represents the liquid phase saturation, and the solid and dashed lines represent the values for the immiscible and miscible states, respectively.

The bound water saturation (S_{wc}) and residual gas saturation (S_{gc}), as input parameters, were each set to 0.1. The minimum and maximum pore radius (r_{min} and r_{max}) are 5 nm and 1,000 nm, respectively. Then for the immiscible state, the residual oil saturation S_{oc} was calculated to be 0.115 according to the values of S_{wc}, r_{max}, and r_c, which resulted in a residual liquid phase saturation , S_{Lc}, of ~ 0.215. When the mixture is completely miscible, S_{oc} and S_{gc} decrease to 0, and the residual liquid saturation S_{Lc_mis} approaches 0.1. The maximum relative permeability increases to only 0.9 since the water phase is immobile.

3.3. Sensitivity analysis

We evaluated the computational accuracy of the proposed model for predictions of fluid density and viscosity. Then, the changes of the relative permeability are then reported relative to pore structure parameters, including the fractal dimension (D_f), the average (r_{mean}) and critical (r_c) pore radius. The near-miscible interpolation was studied by modeling the multiple contact miscibility (MCM) process. The effects of the pressure and nanopore confinement on the system composition are
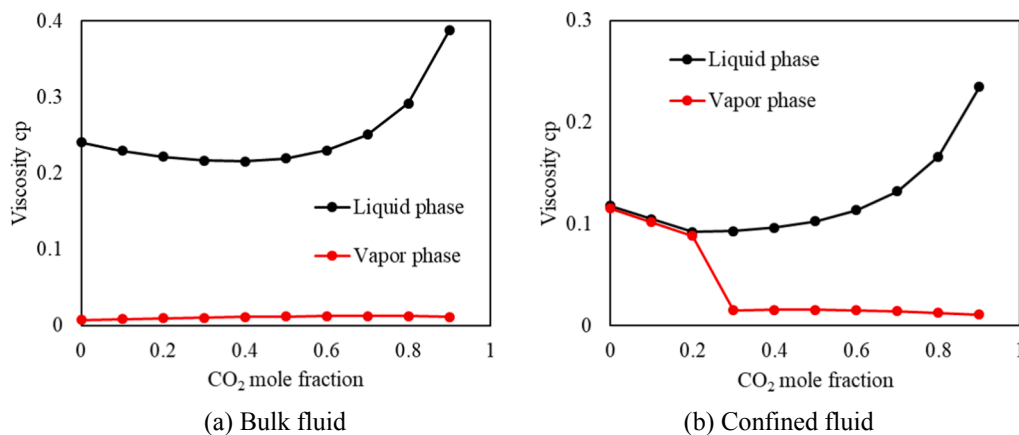

(a) CO_2 density

(b) C_{12} density

Fig. 5. Changes in CO_2 and C_{12} density with pressure for the bulk and confined fluids.

(a) Bulk fluid   (b) Confined fluid

Fig. 6. Changes in *in situ* oil viscosity with CO_2 mole fraction in both bulk and confined fluids.
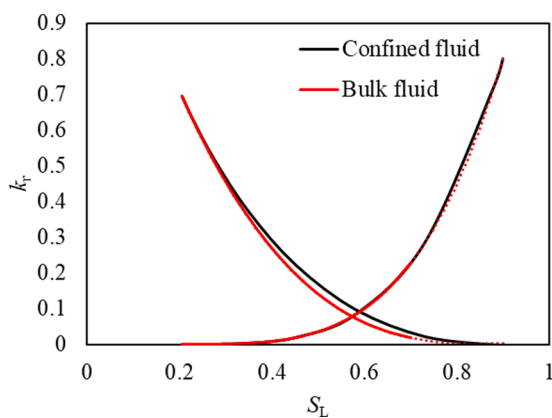

Fig. 7. Effect of mean pore size, r_{mean}, on relative permeability.
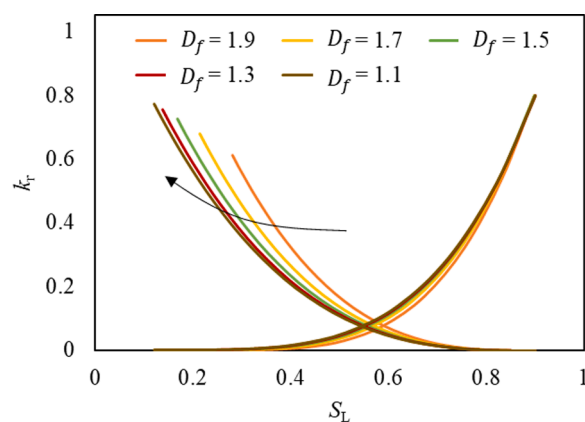

Fig. 8. Effect of fractal dimension, D_f, on relative permeability.

discussed in detail. The relative permeability endpoints are obtained by the GFE-based interpolation according to the two reference states in Fig. 4.

3.3.1. Calculation of the fluid density and viscosity

CO_2 flooding in porous media is significantly affected by the density and viscosity of the vapor and liquid phases. Fig. 5 compares the measured CO_2 and alkane density measurements against calculations from the proposed model at reservoir temperature (255 °F). The observational data are obtained from the NIST Chemistry WebBook [46] (green diamonds, Fig. 5) and calculations for the bulk fluid in conventional macropores or cracks (with an average pore radius, r_{mean}, $\geq 1 \times 10^5$ nm) are shown as solid red lines. Meanwhile, the results for assumed nanopore confinement of the fluid (with $r_{mean} = 5$ nm) are shown as the solid blue lines. The calculated results for the non-hydrocarbon (CO_2) and heavy hydrocarbon (C_{12}) phases agree closely with the observational data for unconfined fluids. However, the densities of the CO_2 and heavy alkane, C_{12}, at high pressure and under nanopore confinement differ significantly and are lower than the bulk fluid – a difference that is important to accommodate.

The vapor–liquid viscosity ratio also exerts a significant impact on relative permeability [69]. Fig. 6 shows the changes of the vapor and liquid viscosities of the bulk and confined fluid with the CO_2 mole fraction. The smaller viscosity difference of the confined fluid (in Fig. 6 (b)) relative to that of the bulk fluid (in Fig. 6 (a)) indicates that the nanopores contribute to an increased mobility ratio. Moreover, when the mole fraction of CO_2 is lower than ~ 0.3, the fluids only exist in a liquidus state within the nanopores, whereas the vapor and liquid phase coexist in the larger pores. This phenomenon demonstrates that

nanopores can reduce the VLE constant of the CO_2, consistent with our previous studies [70].

3.3.2. Factors influencing immiscible relative permeability

The differences in the calculated density and viscosity will inevitably impact the relative permeability, through the pore size, as shown in Fig. 7. The x-ordinate is the saturation of the wetting phase, which is the liquid phase in this work. The red and black lines represent the bulk fluid and the confined fluid relative permeabilities, respectively. Moreover, the initial liquid saturation of the bulk fluid (of ~ 0.75) is lower than that of the confined fluid (of ~ 0.9), which is due to the difference in the VLE. Thus, relative permeabilities beyond the initial liquid saturation in the figure are indicated by the red dotted line. A decrease in the pore size has a negligible effect on the wetting phase relative permeability; however, it will increase the relative permeability of the non-wetting phase (vapor phase) and result in a shift to the left (reduced liquid saturation) of the isosmotic point.

Fractal dimension, D_f, relates to the degree of the pore structure disorder. In this work, D_f ranges from 1.1 to 1.9 to represent the disordered characteristics of the capillary distribution within the cross-section of the representative elementary volume (REV). As described in Eqs. (46)–(51), changing D_f affects the pore size distribution and the total number of pores; thus, it changes the single-phase flux and phase saturation. The average pore radius, r_{mean}, will increase with a decrease in D_f, according to the probability density function of Eq. (47). Therefore, the properties of the confined fluid should be correspondingly modified according to Eqs. (1)–(3). As shown in Fig. 8, a decrease in D_f (reduction in disorder) will result in a decline in the vapor phase relative permeability and an increase in the liquid phase relative permeability,
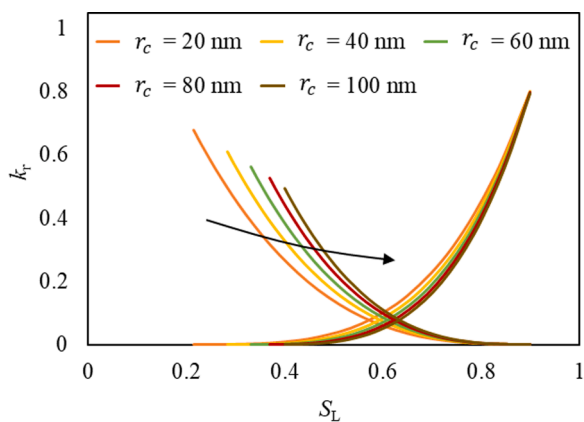
Fig. 9. Effect of critical pore radius r_c on relative permeability.

and a shift in the isosmotic point to the left (lower liquid saturation). Since the VLE in the confined space is affected by the average pore size (r_{mean}), which in turn is a function of D_f, the variation of the relative permeability in Fig. 8 results from the combined effects of the fluid properties and the change in architecture of the pore structure.

The critical pore radius, r_c, is set to be the minimum pore radius that invading fluid can displace. This parameter relates to the pore connectivity and can be measured through mercury injection porosimetry or by imaging via NMR or X-ray CT [71]. With an increase in r_c, the vapor phase relative permeability increases significantly, whereas the liquid phase permeability slightly decreases. The isosmotic point and the relative permeability endpoints move to the right (as shown in Fig. 9). In

addition, as the system approaches miscibility during the CO_2 displacement, a reduction in the interfacial tension can be reflected in the model by reducing r_c; hence, the endpoints can gradually move from the initial calculation to the zero point. The value of r_c at the reference points can be obtained by performing experiments or logging data, while its variation in the near-miscible phase can be obtained by interpolation.

3.3.3. Factors influencing GFE-based interpolations

This section describes the cell-to-cell simulations that used the modified volume translated Peng-Robinson and expanded fluid based correlation (VTPR + EFB) model to present the process of reaching miscibility through multiple contacts (Figs. 10 and 13-14 (a)). The normalized Gibbs Free Energy (NGFE) of the vapor and liquid phases at each test point was calculated to determine whether the model is running correctly under the near-miscible condition. The fractal dimension, D_f, was 1.7 and the critical pore radius, r_c, was 20 nm. The average pore radius, r_{mean}, was then calculated to be 11.85 nm. The calculation (Fig. 10) was conducted at 3,500 psi, where the bulk fluid CO_2 and the *in situ* oil are theoretically considered to be in multiple contact miscibility (MCM). Fig. 10 (a) shows the path of the composition before the interfacial tension decreases to zero. Correspondingly, the NGFE of the vapor and liquid phase (in Fig. 10 (b)) gradually becomes consistent as the system composition changes. For the backward process with CO_2 injection, the molar fraction of hydrocarbon components decreases, the liquid phase NGFE increase while the vapor phase NGFE decrease, leading to the rise of the interpolation parameter F_k (Fig. 11 (a)). The relative permeability parameters keep moving toward the reference point for the immiscible state (Fig. 11 (b)).

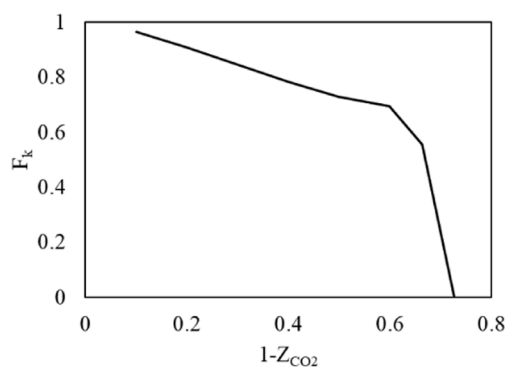As the system pressure decreases, the vapor and liquid NGFE move
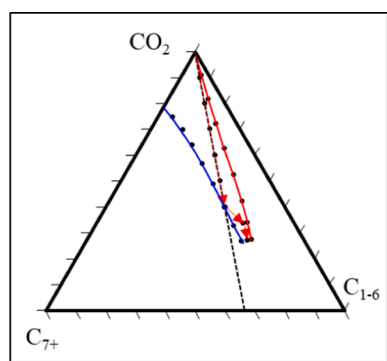
(a) Multiple contact calculations
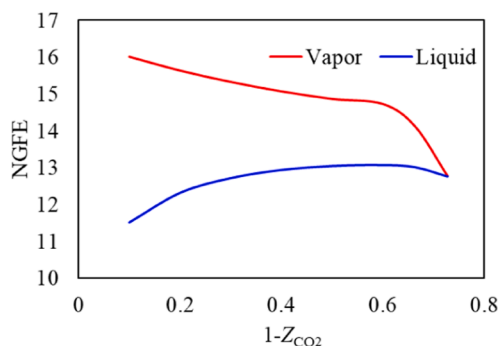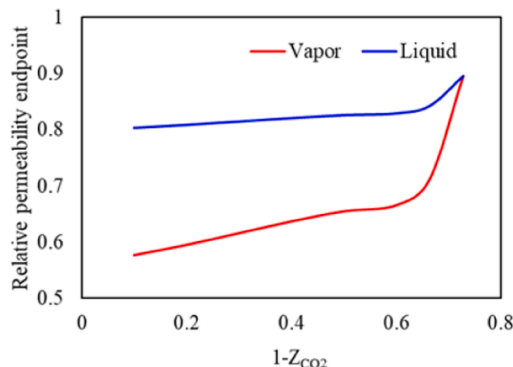

(b) Normalized Gibbs free energy (GFE)

Fig. 10. Evaluation of (a) multiple contact miscibility (MCM) and (b) the corresponding normalized Gibbs Free Energy (NGFE) for the bulk fluid at 3,500 psi.

(a) Interpolation parameter F_k

(b) Relative permeability endpoint

Fig. 11. Changes in the F_k (a) and the relative permeability endpoint (b) with hydrocarbon mole fraction.
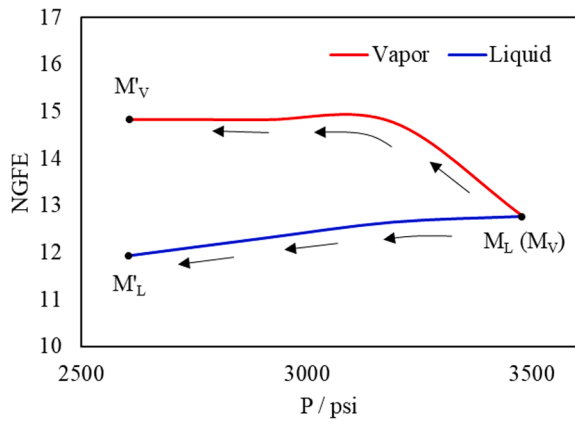
Fig. 12. Changes in the normalized Gibbs Free Energy (NGFE) with pressure.

from the same point M to point M'_V and point M'_L, respectively (as shown in Fig. 12). The increasing difference between the two NGFEs indicates the deviation of the system from the miscible state. Then, the endpoints can be interpolated by using Eqs. (62) and (63). When the pressure is reduced to ~ 2600 psi, the interpolation parameter F_k tends to stabilize at ~ 0.9 (Fig. 13 (a)), resulting in the relative permeability parameters almost unchanged (as shown in Fig. 13 (b)). The vapor phase endpoint drops to ~ 0.6, and the liquid phase endpoint drops to ~ 0.8, corresponding to liquid phase saturations of 0.26 and 0.9, respectively. This is because, under the immiscible state, the NGFE ratio of liquid and vapor phase (so as the F_k) remains almost unchanged with a stable chemical potential difference. Constrained by the setting of the irreducible water

saturation (which is 0.1), the endpoint in the miscible state is ~ 0.9 (Fig. 13 (b)).

Specifically, when the pressure drops to 2,900 psi, the bulk fluid composition changes paths, and the flash calculation results are shown in Fig. 14. The system cannot reach the miscible state by changing the fluid composition. Thus, interfacial tension always exists between the vapor and liquid phases, and there is no intersection point between the NGFE of the two phases. However, when we consider the effect of the confined space on the fluid properties, miscibility occurs in the CO_2 system and the *in situ* oil, as shown in Fig. 15. The comparison reveals the composition changes to the bulk and confined fluid at the same temperature and pressure. The compositional changes are further reflected in the relative permeability through continuous changes of the NGFE, as shown in Fig. 16. The x-ordinate represents the ratio of the CO_2 molar fraction and at the critical point. The NGFE at the critical point was calculated to be 14.11 to conduct interpolation for the single-phase region. Since the process in Fig. 15 only involves interpolation within the two-phase region, we can apply Eq. (63a) for the calculation. Since the components approach the critical point, the endpoint values of the relative permeability of the vapor and liquid phase become equal at 0.9.

This model can be integrated with a compositional simulator to address field-scale problems but incorporate the important micro-scale physics of unconventional reservoirs. The rapid recovery of a fraction of the wetting fluid via displacement can be well represented. However, after displacement-dominated transport terminates, the remaining liquid is trapped in the pore and becomes stagnant – then evaporative transport initiates and becomes progressively more conspicuous [72]. In a transport state that is dominated by evaporation, the liquid evaporates into the injected CO_2 and is removed as a wet gas with a high hydrocarbon content along with the vapor mixture. Then, the vapor

(a) Interpolation parameter F_k

(b) Relative permeability endpoint
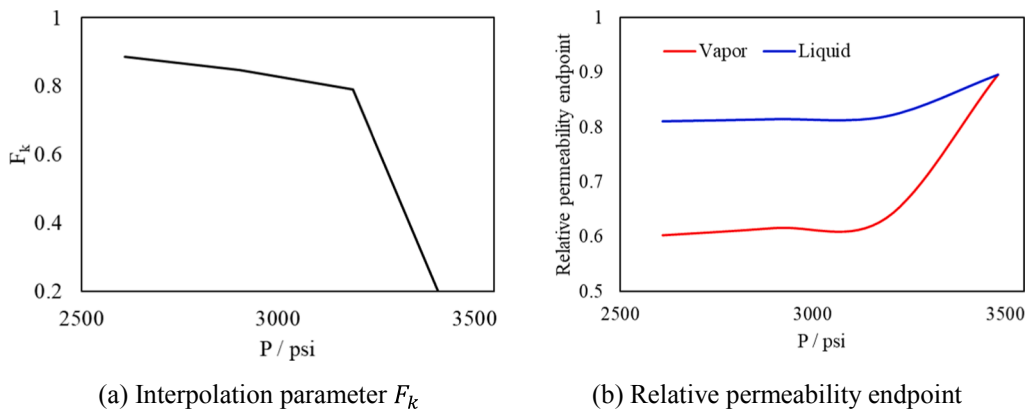
Fig. 13. Changes in the F_k (a) and the relative permeability endpoint (b) with pressure.

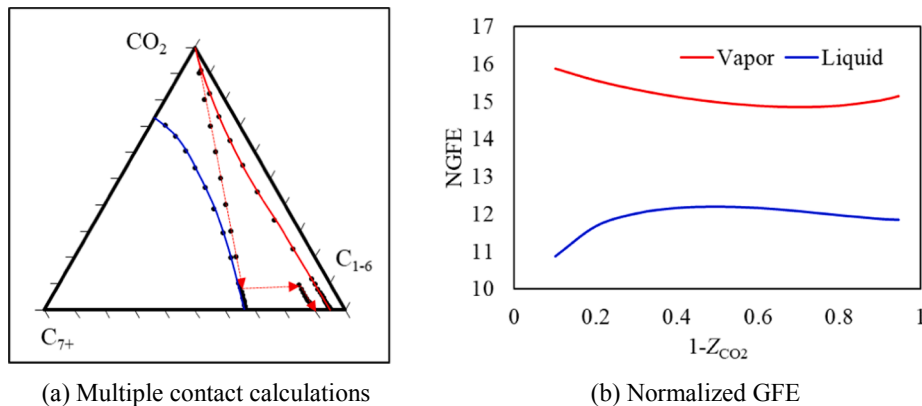(a) Multiple contact calculations

(b) Normalized GFE

Fig. 14. Evaluation of (a) multiple contact miscibility (MCM) and (b) the corresponding normalized Gibbs Free Energy (NGFE) for the bulk fluid at 2,900 psi.

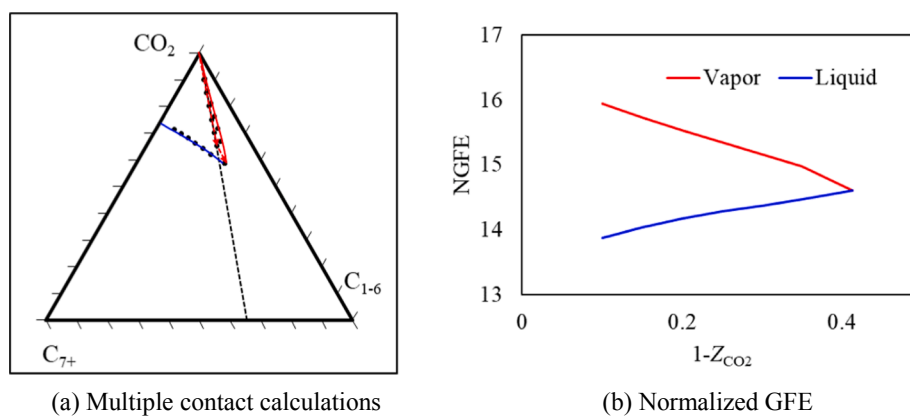(a) Multiple contact calculations　　　　　　　(b) Normalized GFE

Fig. 15. Evaluation of (a) multiple contact miscibility (MCM) and (b) the corresponding normalized Gibbs Free Energy (NGFE) for the confined fluid at 2,900 psi.
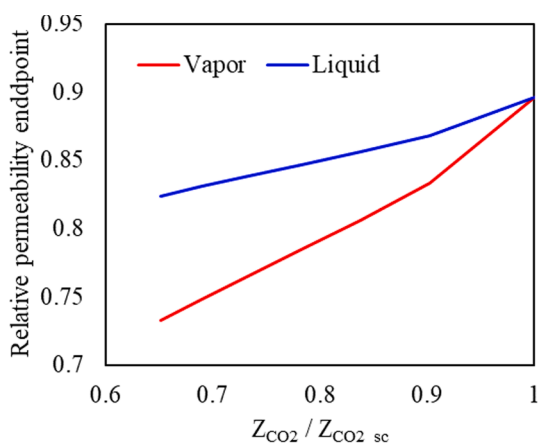

Fig. 16. Changes in the relative permeability endpoint when approaching miscibility.

permeability increases with continuing CO_2 injection, whereas the liquid phase is immobile within the porous medium. A further modification of the relative permeability model is necessary to simulate the evaporation-dominated transport during CO_2 flooding.

4. Conclusions

The combination of the volume translated Peng-Robinson model with the expanded fluid based correlation method (VTPR + EFB) can be used to calculate the density, viscosity, and phase equilibrium of multiphase fluid mixtures at high temperature and high pressure in unconventional reservoirs, and within a permissible error. Based on this, the proposed new relative permeability model can consider the dynamics of CO_2-oil diffusion and oil–water interface slip in nanometer-scale pores. This provides a basis for appropriately and effectively integrating microscale effects of the physics of fluid transmission into field-scale compositional simulation. The following conclusions can be drawn.

1. Accommodating the additional resistance of the pore wall to the wetting phase, renders the relative permeability calculation more consistent with the experimental results. The additional resistance factor β_R is equivalent to the reciprocal of the wetting phase saturation S_{wet}, as determined from the fitting of results in this study.

2. To ensure that all the interpolations during CO_2 flooding fall within prescribed limits, the reference point for the Gibbs Free Energy (GFEs) representing near-miscible relative permeability can be selected as: 1) the value for the injected CO_2 (16.89) at the FCM pressure (4,700 psi), and 2) the value of the separated oil (5.977) at the bottom hole pressure (1,500 psi) of the producing well.

3. Nanopore confinement reduces the density of both the hydrocarbon and non-hydrocarbon components and increases the vapor–liquid viscosity ratio. As a result, the non-wetting phase relative permeability will increase while the wetting phase relative permeability remains almost unchanged.

4. The relative permeability of the non-wetting phase (vapor phase) is more sensitive to the change in the key parameters of the proposed model, as compared to the wetting phase. An increase in the fractal dimension D_f and the critical pore radius r_c will result in an increase in the vapor phase relative permeability and a decline in the liquid phase permeability.

5. Confined fluids can achieve miscibility at lower pressures. Within the range of the reference points, the NGFE values can reflect the variation of the proximity to miscibility that is caused by the pore size and pressure. The interpolation algorithm, based on the NGFE, has been shown to provide accurate representation even local to the critical point.

CRediT authorship contribution statement

Mingyu Cai: Investigation, Data curation, Methodology, Writing – original draft. **Yuliang Su:** Supervision. **:** . **Shiyuan Zhan:** Methodology. **Derek Elsworth:** Supervision, Writing – review & editing. **Lei Li:** Investigation.

Declaration of Competing Interest

The authors declare that they have no known competing financial interests or personal relationships that could have appeared to influence the work reported in this paper.

Acknowledgments

Appendix

Table 1

Mole percentages and properties of the different components in hydrocarbons recovered from the Wolfcamp formation.

NO.	Component	T_c K	P_c atm	a_c	v_c L/mol	P_c/T_c Ref. [8]	P_c/T_c Ref. [38]	Deviation	T_c' K	P_c' atm
CO_2	/	304.2	72.8	0.228	44.01	3.7	0.043	252.5	283.6	67.9
C_1	0.338	186.3	44.6	0.010	16.54	2.2	0.043	147.8	171.2	41.0
C_2	0.088	305.5	49.1	0.103	30.43	5.5	0.064	247.2	276.7	44.5
C_3	0.097	370.0	41.9	0.152	44.10	9.4	0.091	302.4	330.5	37.4
C_4	0.060	421.8	37.2	0.189	58.12	13.8	0.116	347.4	372.6	32.8
C_{5-6}	0.088	486.4	31.4	0.268	78.30	21.7	0.159	407.1	422.6	27.3
C_{7-12}	0.189	585.1	24.7	0.429	120.56	39.9	0.243	505.6	494.4	20.9
C_{13-21}	0.077	740.1	17.0	0.720	220.72	92.8	0.447	676.0	592.5	13.6
C_{22-80}	0.062	1024.7	12.9	1.016	443.51	233.6	0.812	987.3	764.5	9.7

Table 2

Binary-interaction parameters used in the flash calculation.

	CO_2	C_1	C_2	C_3	C_4	C_{5-6}	C_{7-12}	C_{13-21}	C_{22-80}
CO_2	0	0.0279	0.0682	0.0701	0.0806	0.0697	0.0643	0.0597	0.057
C_1	0.0279	0	0.005	0.0035	0.0035	0.0037	0.0033	0.0033	0.0033
C_2	0.0682	0.005	0	0.0031	0.0031	0.0031	0.0026	0.0026	0.0026
C_3	0.0701	0.0035	0.0031	0	0	0	0	0	0
C_4	0.0806	0.0035	0.0031	0	0	0	0	0	0
C_{5-6}	0.0697	0.0037	0.0031	0	0	0	0	0	0
C_{7-12}	0.0643	0.0033	0.0026	0	0	0	0	0	0
C_{13-21}	0.0597	0.0033	0.0026	0	0	0	0	0	0
C_{22-80}	0.057	0.0033	0.0026	0	0	0	0	0	0

References

[1] Cheng Z, Ning Z, Kang D-H. Lattice Boltzmann simulation of water flow through rough nanopores. Chem Eng Sci 2021;236:116329. https://doi.org/10.1016/j.ces.2020.116329.

[2] Law BE, Curtis J. Introduction to unconventional petroleum systems. AAPG Bull 2002;86(11):1851–2.

[3] Jin L, Hawthorne S, Sorensen J, Pekot L, Kurz B, Smith S, et al. Advancing CO2 enhanced oil recovery and storage in unconventional oil play—experimental studies on Bakken shales. Appl Energy 2017;208:171–83.

[4] Assef Y, Kantzas A, Pereira Almao P. Numerical modelling of cyclic CO2 injection in unconventional tight oil resources; trivial effects of heterogeneity and hysteresis in Bakken formation. Fuel 2019;236:1512–28.

[5] Cai M, Su Y, Hao Y, Guo Y, Elsworth D, Li L, et al. Monitoring oil displacement and CO2 trapping in low-permeability media using NMR: a comparison of miscible and immiscible flooding. Fuel 2021;305:121606. https://doi.org/10.1016/j.fuel.2021.121606.

[6] Alharthy NS, Nguyen TN, Teklu TW, Kazemi H, Graves RM. Multiphase compositional modeling in small-scale pores of unconventional shale reservoirs. In: SPE annual technical conference and exhibition. OnePetro; 2013.

[7] Jiao K, Yao S, Liu C, Gao Y, Wu H, Li M, et al. The characterization and quantitative analysis of nanopores in unconventional gas reservoirs utilizing FESEM–FIB and image processing: an example from the lower Silurian Longmaxi Shale, upper Yangtze region, China. Int J Coal Geol 2014;128–129:1–11.

[8] Chen M, Cheng L, Wang X, Lyu C, Cao R. Pore network modelling of fluid flow in tight formations considering boundary layer effect and media deformation. J Petrol Sci Eng 2019;180:643–59.

[9] Islam AW, Patzek TW, Sun AY. Thermodynamics phase changes of nanopore fluids. J Nat Gas Sci Eng 2015;25:134–9.

[10] Sang G, Liu S, Zhang R, Elsworth D, He L. Nanopore characterization of mine roof shales by SANS, nitrogen adsorption, and mercury intrusion: impact on water adsorption/retention behavior. Int J Coal Geol 2018;200:173–85.

[11] Wang F, Zhao J. Mathematical modeling of gravity and buoyancy effect on low interfacial tension spontaneous imbibition in tight oil reservoirs. AIChE J 2021;67 (9). https://doi.org/10.1002/aic.v67.910.1002/aic.17332.

[12] Zhang T, Javadpour F, Yin Y, Li X. Upscaling water flow in composite nanoporous shale matrix using lattice Boltzmann method. Water Resour Res 2020;56(4). https://doi.org/10.1029/2019WR026007.

[13] Lowry E, Piri M. Effects of chemical and physical heterogeneity on confined phase behavior in nanopores. Microporous Mesoporous Mater 2018;263:53–61.

[14] Sang G, Liu S, Elsworth D, Yang Y, Fan L. Evaluation and modeling of water vapor sorption and transport in nanoporous shale. Int J Coal Geol 2020;228:103553. https://doi.org/10.1016/j.coal.2020.103553.

[15] Feng D, Wu K, Wang X, Li J, Li X. Modeling the confined fluid flow in micro-nanoporous media under geological temperature and pressure. Int J Heat Mass Transf 2019;145:118758. https://doi.org/10.1016/j.ijheatmasstransfer.2019.118758.

[16] Sheng G, Javadpour F, Su Y. Effect of microscale compressibility on apparent porosity and permeability in shale gas reservoirs. Int J Heat Mass Transf 2018;120: 56–65.

[17] Li J, Chen ZJ, Lei Z, Gao Y, Yang S, Wu W, et al. Modelling the apparent viscosity of water confined in nanoporous shale: effect of the fluid/pore-wall interaction. In:

[18] SPE Annual Technical Conference and Exhibition. Day 3 Wed, October 28, 2020; 2020.

[19] Wang H, Chen L, Qu Z, Yin Y, Kang Q, Yu B, et al. Modeling of multi-scale transport phenomena in shale gas production—a critical review. Appl Energy 2020;262: 114575. https://doi.org/10.1016/j.apenergy.2020.114575.

[20] Li Y, Kalantari-Dahaghi A, Zolfaghari A, Dong P, Negahban S, Zhou D. Fractal-based real gas flow model in shales: an interplay of nano-pore and nano-fracture networks. Int J Heat Mass Transf 2018;127:1188–202.

[21] Li R, Chen Z, Wu K, Liu X, Dou L, Yang S, et al. A fractal model for gas-water relative permeability curve in shale rocks. J Nat Gas Sci Eng 2020;81:103417. https://doi.org/10.1016/j.jngse.2020.103417.

[22] Alhosani A, Lin Q, Scanziani A, Andrews E, Zhang K, Bijeljic B, et al. Pore-scale characterization of carbon dioxide storage at immiscible and near-miscible conditions in altered-wettability reservoir rocks. Int J Greenhouse Gas Control 2021;105:103232. https://doi.org/10.1016/j.ijggc.2020.103232.

[23] Alzayer AN, Voskov DV, Tchelepi HA. Relative permeability of near-miscible fluids in compositional simulators. Transp Porous Media 2018;122(3):547–73.

[24] Zhang Y, Lebedev M, Jing Y, Yu H, Iglauer S. In-situ X-ray micro-computed tomography imaging of the microstructural changes in water-bearing medium rank coal by supercritical CO2 flooding. Int J Coal Geol 2019;203:28–35.

[25] Wei B, Zhang X, Wu R, Zou P, Gao K, Xu X, et al. Pore-scale monitoring of CO2 and N2 flooding processes in a tight formation under reservoir conditions using nuclear magnetic resonance (NMR): a case study. Fuel 2019;246:34–41.

[26] Ghanbarian B, Liang F, Liu H-H. Modeling gas relative permeability in shales and tight porous rocks. Fuel 2020;272:117686. https://doi.org/10.1016/j.fuel.2020.117686.

[27] Khorsandi S, Li L, Johns RT. A new way of compositional simulation without phase labeling. SPE J 2021;26(02):940–58.

[28] Neshat SS, Pope GA. Compositional three-phase relative permeability and capillary pressure models using Gibbs free energy. In: SPE reservoir simulation conference. OnePetro; 2017.

[29] Jerauld G. General three-phase relative permeability model for Prudhoe Bay. SPE Reservoir Eng 1997;12(04):255–63.

[30] Khebzegga O, Iranshahr A, Tchelepi H. Continuous relative permeability model for compositional simulation. Transp Porous Media 2020;134(1):139–72.

[31] Wang C, Lu H, Wang Z, Xiu P, Zhou B, Zuo G, et al. Stable liquid water droplet on a water monolayer formed at room temperature on ionic model substrates. Phys Rev Lett 2009;103(13). https://doi.org/10.1103/PhysRevLett.103.137801.

[32] Zhu C, Li H, Huang Y, Zeng XC, Meng S. Microscopic insight into surface wetting: relations between interfacial water structure and the underlying lattice constant. Phys Rev Lett 2013;110(12):126101.

[33] Zhan S, Su Y, Jin Z, Wang W, Li L. Effect of water film on oil flow in quartz nanopores from molecular perspectives. Fuel 2020;262:116560. https://doi.org/10.1016/j.fuel.2019.116560.

[34] Zhan S, Su Y, Jin Z, Wang W, Li L. Oil-water two-phase flow behavior in shale inorganic nanopores: from molecule level to theoretical mathematical model. In: Unconventional resources technology conference, 20–22 July 2020. Unconventional Resources Technology Conference (URTEC); 2020. p. 3749–62.

[35] Ahlers J, Gmehling J. Development of an universal group contribution equation of state: I. Prediction of liquid densities for pure compounds with a volume translated Peng-Robinson equation of state. Fluid Phase Equilib 2001;191(1–2):177–88.

[36] Mathias PM, Naheiri T, Oh EM. A density correction for the Peng—Robinson equation of state. Fluid Phase Equilib 1989;47(1):77–87.

[36] Abudour AM, Mohammad SA, Robinson RL, Gasem KAM. Volume-translated Peng-Robinson equation of state for liquid densities of diverse binary mixtures. Fluid Phase Equilib 2013;349:37–55.

[37] Chou GF, Prausnitz JM. A phenomenological correction to an equation of state for the critical region. AIChE J 1989;35(9):1487–96.

[38] Peng D-Y, Robinson DB. A new two-constant equation of state. Ind Eng Chem Fundam 1976;15(1):59–64.

[39] Bian B, Wang Y, Shi J. Parameters for the PR and SRK equations of state. Fluid Phase Equilib 1992;78:331–4.

[40] Abudour AM, Mohammad SA, Robinson RL, Gasem KAM. Volume-translated Peng-Robinson equation of state for saturated and single-phase liquid densities. Fluid Phase Equilib 2012;335:74–87.

[41] Chueh PL, Prausnitz JM. Vapor-liquid equilibria at high pressures: Calculation of critical temperatures, volumes, and pressures of nonpolar mixtures. AIChE J 1967; 13(6):1107–13.

[42] Aalto M, Keskinen KI, Aittamaa J, Liukkonen S. An improved correlation for compressed liquid densities of hydrocarbons. Part 2. Mixtures. Fluid Phase Equilib 1996;114(1–2):21–35.

[43] Kesler MG, Robinson DB. Improve prediction of enthalpy of fractions. 1976.

[44] Byung I, Lee BI, MG K. A generalized thermodynamic correlation based on three-parameter corresponding states. 1975.

[45] Satyro MA, Yarranton HW. Expanded fluid-based viscosity correlation for hydrocarbons using an equation of state. Fluid Phase Equilib 2010;298(1):1–11.

[46] Linstrom PJ. NIST chemistry webbook. http://webbook.nist.gov. 2005.

[47] Yarranton HW, Satyro MA. Expanded fluid-based viscosity correlation for hydrocarbons. Ind Eng Chem Res 2009;48(7):3640–8.

[48] Motahhari H, Satyro MA, Yarranton HW. Predicting the viscosity of asymmetric hydrocarbon mixtures with the expanded fluid viscosity correlation. Ind Eng Chem Res 2011;50(22):12831–43.

[49] Wong DSH, Sandler SI. A theoretically correct mixing rule for cubic equations of state. AIChE J 1992;38(5):671–80.

[50] Fukano T, Ousaka A. Prediction of the circumferential distribution of film thickness in horizontal and near-horizontal gas-liquid annular flows. Int J Multiph Flow 1989;15(3):403–19.

[51] Edomwonyi-Otu LC, Angeli P. Pressure drop and holdup predictions in horizontal oil–water flows for curved and wavy interfaces. Chem Eng Res Des 2015;93:55–65.

[52] Yu B. Analysis of flow in fractal porous media. Appl Mech Rev 2008;61(5):050801. https://doi.org/10.1115/1.2955849.

[53] Yu B, Li J. Some fractal characters of porous media. Fractals 2001;09(03):365–72.

[54] Ransohoff TC, Radke CJ. Laminar flow of a wetting liquid along the corners of a predominantly gas-occupied noncircular pore. J Colloid Interface Sci 1988;121(2): 392–401.

[55] Xu P, Qiu S, Yu B, Jiang Z. Prediction of relative permeability in unsaturated porous media with a fractal approach. Int J Heat Mass Transf 2013;64:829–37.

[56] Iranshahr A. Tie-simplex method for thermal-compositional simulation. Stanford University; 2012.

[57] Yuan C, Pope GA. A new method to model relative permeability in compositional simulators to avoid discontinuous changes caused by phase-identification problems. SPE J 2012;17(04):1221–30.

[58] Wei W, Cai J, Xiao J, Meng Q, Xiao B, Han Q. Kozeny-Carman constant of porous media: insights from fractal-capillary imbibition theory. Fuel 2018;234:1373–9.

[59] Song W, Wang D, Yao J, Li Y, Sun H, Yang Y, et al. Multiscale image-based fractal characteristic of shale pore structure with implication to accurate prediction of gas permeability. Fuel 2019;241:522–32.

[60] Wang H, Su Y, Wang W, Li L, Sheng G, Zhan S. Relative permeability model of oil-water flow in nanoporous media considering multi-mechanisms. J Petrol Sci Eng 2019;183:106361. https://doi.org/10.1016/j.petrol.2019.106361.

[61] Chen KE, Chen HE, Xu P. A new relative permeability model of unsaturated porous media based on fractal theory. Fractals 2020;28(01):2050002. https://doi.org/10.1142/S0218348X20500024.

[62] Borazjani S, Hemmati N, Behr A, Genolet L, Mahani H, Zeinijahromi A, et al. Determining water-oil relative permeability and capillary pressure from steady-state coreflood tests. J Petrol Sci Eng 2021;205:108810. https://doi.org/10.1016/j.petrol.2021.108810.

[63] Chen L, Kang Q, Mu Y, He Y-L, Tao W-Q. A critical review of the pseudopotential multiphase lattice Boltzmann model: Methods and applications. Int J Heat Mass Transf 2014;76:210–36.

[64] Oak M, Baker L, Thomas D. Three-phase relative permeability of Berea sandstone. J Petrol Technol 1990;42(08):1054–61.

[65] Oren P-E, Bakke S, Arntzen OJ. Extending predictive capabilities to network models. SPE J 1998;3(04):324–36.

[66] Li L, Sheng JJ, Su Y, Zhan S. Further investigation of effects of injection pressure and imbibition water on CO2 huff-n-puff performance in liquid-rich shale reservoirs. Energy Fuels 2018;32(5):5789–98.

[67] Pederson K, Fjellerup J, Thomassen P, Fredenslund A. Studies of gas injection into oil reservoirs by a cell-to-cell simulation model. In: SPE Annual Technical Conference and Exhibition. OnePetro; 1986.

[68] Ahmadi K, Johns RT. Multiple-mixing-cell method for MMP calculations. SPE J 2011;16(04):733–42.

[69] Blom S, Hagoort J, Soetekouw D. Relative permeability at near-critical conditions. SPE J 2000;5(02):172–81.

[70] Cai M, Su Y, Elsworth D, Li L, Fan L. Hydro-mechanical-chemical modeling of sub-nanopore capillary-confinement on CO2-CCUS-EOR. Energy 2021;225:120203. https://doi.org/10.1016/j.energy.2021.120203.

[71] Wang L, Zhao N, Sima L, Meng F, Guo Y. Pore structure characterization of the tight reservoir: systematic integration of mercury injection and nuclear magnetic resonance. Energy Fuels 2018;32(7):7471–84.

[72] Lu M, Connell LD, Pan Z. Wetting fluid behaviour with phase transition in geological nanopores: Liquid film, capillary condensation and evaporative flow. J Petrol Sci Eng 2020;195:107570. https://doi.org/10.1016/j.petrol.2020.107570.